

ON THE EFFECTS OF TURBULENCE MODELING AND GRID REFINEMENT ON HIGH-LIFT CONFIGURATION AERODYNAMIC SIMULATIONS

Alexandre P. Antunes^{*}, Ricardo Galdino da Silva[†], João Luiz F. Azevedo[‡]

^{*} Instituto Tecnológico de Aeronáutica, ITA (ap-antunes@uol.com.br)

[†] Universidade de São Paulo, USP (ricardo.galdino@poli.usp.br)

[‡] Instituto de Aeronáutica e Espaço, DCTA/IAE/ALA (joaoluiz.azevedo@gmail.com)

Keywords: *CFD, High-Lift Configuration, Trapezoidal Wing, Aerodynamic Design*

Abstract

The paper presents simulations over a trapezoidal wing with a single slotted flap and a slat. The calculations are performed for the high-lift configuration known as configuration one, which is characterized by slat and flap deflections of 30° and 25°, respectively. The simulations address both the actual configuration tested, with the supporting brackets for the high-lift devices, as well as a simplified configuration without the brackets. Both hybrid tetrahedral-prismatic and hexahedral meshes are considered in the calculations. For the purpose of analyzing the effect of the turbulence model, simulations are performed using the Spalart-Allmaras, Menter SST and cubic $k-\epsilon$ turbulence models. The grids for the configuration without brackets range from 12 million to 22.8 million cells, whereas for the configuration with the brackets the grids vary from 24.8 million, for the coarse mesh, to 69.5 million cells, for the fine mesh.

1 Introduction

Computational Fluid Dynamics (CFD) has been consolidated as a quite mature science along the last 30 to 40 years of development [1, 2]. Nowadays, CFD is a well-know technology, deeply inserted into aerodynamic groups to perform the most diverse types of analyses. The paper presents three-dimensional simulations over

the NASA Trapezoidal Wing [3, 4]. This semi-span model has been tested both in the NASA Ames 12-Foot Pressurized Tunnel (PWT) and the NASA Langley 14 by 22 Foot Subsonic Wind Tunnel (SWT). The model was developed to provide a database for CFD validation. The calculations here reported consider, initially, the configuration known as configuration one, which is characterized by the slat and flap deflections of 30 deg. and 25 deg., respectively.

In order to perform the present study, two mesh generation approaches are selected. The first one considers the generation of hybrid tetrahedral-prismatic meshes for the configuration with the supporting brackets, and the second one relies in the generation of both hexahedral and hybrid tetrahedral-prismatic meshes for the configuration without the brackets. The reason for not adopting the hexahedral methodology to generate the meshes over the configuration with the supporting brackets resides in the complexity that these components bring into the mesh generation process.

Previous work [5, 6] by the present authors has already addressed simulations for the Trap Wing configuration, and the present paper intends to extend on those previous studies including new set of results. The first set builds upon the previous obtained results with the hexahedral meshes, but in this case, considering the adoption of different turbulence models into the nu-

merical simulation. The second set of results are focused in the effects of the supporting brackets over the obtained aerodynamic coefficients. Moreover, the paper also considers the sensitivity of these aerodynamic coefficients with respect to a surface and a spatial mesh refinement. Details about the mesh refinement, for the hybrid meshes, are discussed in the forthcoming sections of the present work. The simulations are performed for several angles of attack and using different turbulence models.

High-lift devices are intrinsically complex lifting components, that generate flow patterns with a vast range of physical phenomena [7, 8, 9]. On such devices, one can commonly find boundary layer confluence, sonic regions, detached regions, flow relaminarization, among other phenomena. The capability to numerically capture all these physical phenomena in detail provides confidence on the obtained aerodynamic coefficients. This accuracy is a very important subject during the definitions of the high-lift systems due to the target design requirements that must be achieved to avoid penalties on the airplane performance [10, 11].

2 Methodology

The simulations are performed with the CFD++ commercial package [12]. All the results are obtained using the Reynolds-average Navier-Stokes equations (RANS). As discussed, the Spalart-Allmaras (SA) [13], the Menter SST [14] and the cubic $k - \epsilon$ [15] turbulence closures are adopted in order to conduct a sensitivity study with regard to the turbulence model. In the present case, only the test conditions adopted at the NASA Langley 14 by 22 Foot Subsonic Wind Tunnel (SWT) are used to perform the numerical simulations. These conditions are freestream Mach number of 0.20 and Reynolds number of 4.3 million, based on the model mean aerodynamic chord. Moreover, all computational meshes used in the present study were generated using the ICEM-CFD package [16].

3 Configurations and Mesh Generation

The trapezoidal wing model has been tested both in the NASA Ames 12-Foot Pressurized Tunnel (PWT) and the NASA Langley 14 by 22 Foot Subsonic Wind Tunnel (SWT) as part of the Advanced Subsonic Technology (AST) High-Lift Program, and the Advanced Subsonic Technology (AST) Airframe Noise Program. A considerably large number of high-lift device configurations and deflections was tested to produce the necessary experimental data for validation and development of CFD methods. Figure 1 shows some geometrical details from one of the tested configurations. In the present study, only con-



Fig. 1 NASA wind tunnel and trapezoidal wing model.

figuration *one*, with and without its supporting brackets, is considered in the performed numerical simulations. For further details about the gap-overlap on the multiple element lifting surface, the interested reader is directed to the homepage of the 1st AIAA CFD High Lift Prediction Workshop [17].

The generated meshes have a spherical outside boundary, which is located 50 chords away from the model. Since no wall boundary condition is imposed on the outer boundary, it is not

ON THE EFFECTS OF TURBULENCE MODELING AND GRID REFINEMENT ON HIGH-LIFT CONFIGURATION AERODYNAMIC SIMULATIONS

necessary to reproduce in detail the wind tunnel test section. At this outer boundary of the mesh, the characteristic equations are imposed as boundary conditions. At the mesh symmetry plane, the symmetry boundary condition is imposed. It is worth mentioning that the experimental results are corrected to eliminate the effect of the tunnel wall boundary layer over the aerodynamic coefficients of the configuration. Thus, the application of the above mentioned boundary conditions are appropriate for the performed simulations.

The prismatic mesh layer, for the hybrid grid cases, is generated over the model surface using a geometric law with a growth ratio of 1.15. The generation of hexahedral meshes also follow the same geometric growth rate for the control volumes in the boundary layer. Moreover, the dimensionless wall distance, y^+ , for the first point off the wall is set equal to one, by adjustments on the grid near the wall. This distance is defined based on the flight condition and the expected shear stress on the surface. The y^+ for a wall-bounded flow can be defined as

$$y^+ \equiv \frac{u_* y}{\nu}, \quad (1)$$

where u_* is the friction velocity at the nearest wall, y is the distance to the nearest wall and ν is the local (laminar) kinematic viscosity of the fluid.

The coarse and refined hexahedral meshes, adopted in the previously work [5, 6], are here again selected in order to perform new numerical simulations considering other turbulence models besides the Spalart-Allmaras model. The coarse hexahedral grid has 12 million cells, while the refined grid achieves a total size of 22.8 million cells. In both cases the mesh distribution along the direction normal to the surface follows a geometric law, with a growth ratio of 1.15, which is the same adopted value for the hybrid methodology. It should be pointed out that, for comparison purposes, results for the configuration without the brackets and considering the hybrid mesh generation approach are also included here.

In Fig. 2, it is possible to observe the blocking concept, typical of the hexahedral mesh method-

ology. This concept consists in attributing the edges of the blocks to the surface and boundaries of the geometry, whenever the block is close enough of the geometry. These blocks are responsible for the generation of the surface mesh and the volumetric mesh close to the surface. The blocks that are in regions far from the geometry are only responsible for representing the volumetric mesh. Their edges are attached to the mesh supporting lines. The process just described is the usual approach adopted by the ICEM-CFD [16] solver for hexahedral mesh generation. Figure 3 shows details of the refined hexahedral surface mesh generated over configuration *one* without the brackets.

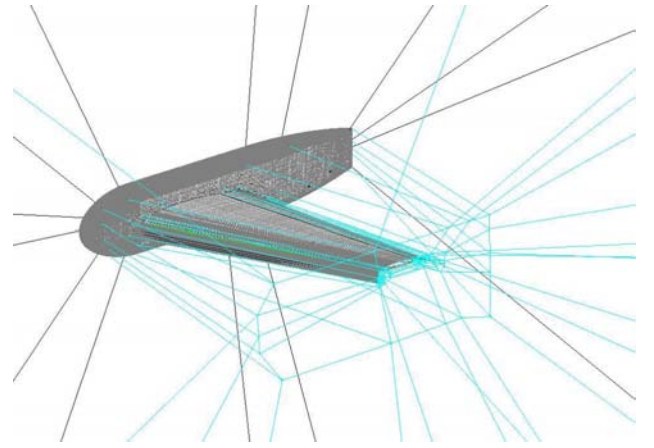


Fig. 2 Block structure necessary in order to define the hexahedral mesh for configuration *one*

In order to perform the second set of simulations, hybrid tetrahedral–prismatic meshes are generated over configuration *one* with its supporting brackets. A study of mesh refinement is conducted considering a baseline grid with 24.8 million cells, a medium grid with 49.3 million cells, and a fine grid with 69.5 million cells. In Fig. 4, one can observe the isometric view of these three meshes. In such study, surface refinement is initially performed and, afterwards, volumetric refinement is conducted for the grid with the finer surface definition.

The surface refinement is accomplished through the imposition of smaller cell sizes, but without allowing that the mesh reference lengths be divided in half. The decision for setting a re-

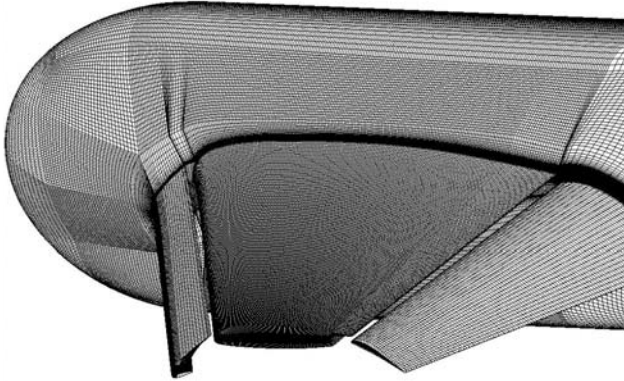
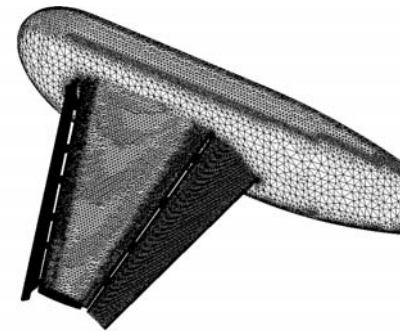


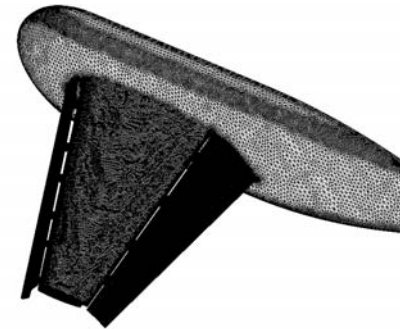
Fig. 3 Hexahedral refined surface mesh for configuration *one*

striction on the decrease of the mesh reference lengths is based in the fact that, otherwise, the number of elements in the final mesh would increase considerably. In terms of spatial refinement, it is decided to select those regions around all the trailing edges of the high-lift system and, also, near the wing-pod junction.

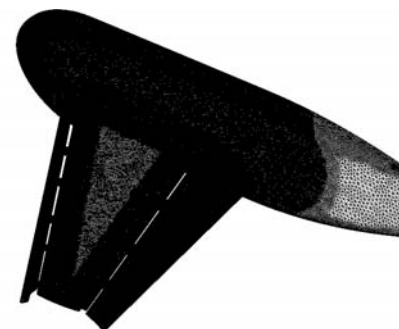
In particular, much of the complexity during the mesh generation process for the configuration with the supporting brackets arises from the proximity of the slat lower surface to the proper supporting bracket rod, as one can observe in Fig. 5. Moreover, the concave shape formed between these two elements and the presence of the bracket base requires special attention in order to setup the most adequate mesh parameters during the mesh generation process. The distance between these geometrical components provides an important information to define the best surface discretization and the prism layer growing characteristics. The lack of awareness of the close proximity of different surfaces of the configuration, at this initial setup stage, can yield some difficulties into the mesh generation process. Actually, they may, sometimes, result in the appearance of negative volumetric elements, which invalidates the use of the obtained mesh. In some extreme cases, the mesh generator aborts the generation procedure due to the impossibility of handling both the geometric constraints and the im-



(a) Coarse Mesh



(b) Medium Mesh



(c) Fine Mesh

Fig. 4 Surface mesh for configuration *one* with its supporting brackets.

posed mesh setup.

In Fig. 6, one can observe a station cut of the volumetric mesh near the slat and flap devices. This station cut plane passes through the first slat and flap brackets. In this figure, the level of volumetric mesh refinement near the wing is quite evident. The fine tetrahedral mesh has a growth ratio, beyond the prismatic mesh layers, which is much slower than the corresponding growth ratio observed for the coarse and medium meshes. This fine mesh was constructed in this fashion

ON THE EFFECTS OF TURBULENCE MODELING AND GRID REFINEMENT ON HIGH-LIFT CONFIGURATION AERODYNAMIC SIMULATIONS

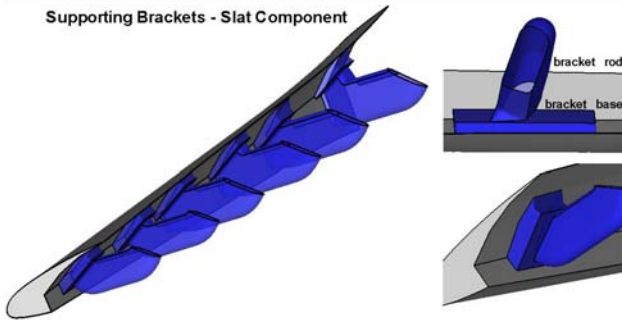


Fig. 5 Bracket details at the slat component of configuration one.

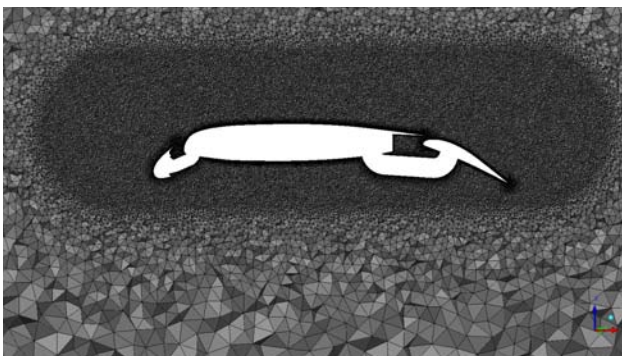


Fig. 6 Station cut over the fine mesh through the mid-plane of the first slat and flap brackets.

in order to attempt to improve capturing of the free shear layers, or detached wakes, that are expected to occur in those regions of the flow in the present calculations. However, the control of this growth ratio, in order to have an adequate volumetric mesh, implies in a considerable increase in the total number of mesh cells.

4 Results

4.1 Configuration Without Supporting Brackets

Figure 7 shows the C_L versus AoA curves obtained by all the simulations performed for the configuration without the brackets. In particular, the authors are interested in the results with the two hexahedral meshes, because these have been used in order to evaluate the effect of the turbulence models in the calculations. Hence, there are results for the SA and SST models, for both

hexahedral meshes, and for the cubic $k - \epsilon$ turbulence model for the refined hexahedral mesh. For comparison purposes, results with the SA model on the baseline hybrid grid (without the brackets) are also shown in this figure.

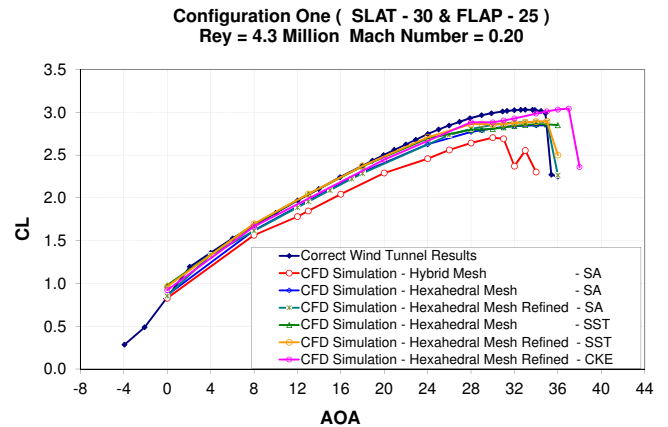


Fig. 7 C_L versus AoA for configuration one.

The results obtained with the SST turbulence model show no difference between the baseline and the refined meshes up to 24 deg. of angle of attack, which consists in the linear part of the curve. Above this angle of attack, the difference between the results with the two meshes do not exceed 0.04 in terms of the C_L coefficient. Typically, at higher angles of attack, the nonlinearities of the flowfield are more pronounced, thus, refined meshes are more adequate to better capture such nonlinearities. The results for the SA model, on the hexahedral meshes, are not much different from those obtained with the SST model. The calculations with the SA model in the baseline hybrid mesh indicate quite poor agreement with the rest of the data in the figure, especially for the higher values of angle of attack. In general, the calculated values of C_{Lmax} are lower than the experimental data. It is interesting to notice that the hexahedral baseline mesh has results that are very similar to those obtained with the refined mesh. This is an indication that the baseline mesh may already be adequate for the intended simulations in the present case.

The other turbulence model used in the present investigation, in order to address simulations for configuration one without the brack-

ets, is the cubic $k - \epsilon$ closure [15]. The results obtained with this model have the same $C_L \times \alpha$ curve slope as those from the simulations performed with the SST model. The results further indicate that the $C_L \times \alpha$ curve for the cubic $k - \epsilon$ model lies below the curve for the SST model, at least for most of the range of angles of attack investigated, for the refined hexahedral mesh. On the other hand, the cubic $k - \epsilon$ model calculations yielded a value of C_{Lmax} which is only slightly larger than the experimental value. However, the stall angle of attack is increased by 2 to 4 deg., when compared to the literature data. The numerical formulation for the cubic $k - \epsilon$ turbulence model considers an explicit nonlinear constitutive relation for the eddy viscosity, which is different, for instance, from the SST model, which has a linear formulation. Such differences may have led the cubic $k - \epsilon$ model to yield a better correlation in the value of C_{Lmax} , but at the expense of delaying the separation and, hence, giving the wrong stall angle of attack.

The drag results for such meshes can be seen in Figs. 8 and 9. The C_L range of interest in the drag polars has been split in two curves in order to allow a better visualization of the results. The results for the drag polars obtained with the SST model are indicating less drag, for the same lift coefficient, when compared to the experimental data. The drag calculations with the cubic $k - \epsilon$ model, for some portions of the C_L range considered, are indicating quite smaller drag coefficients than those indicated by the experimental results.

Results with the SA model and the hexahedral meshes are indicating a very good agreement with the experimental drag coefficients. On the other hand, calculations with the SA model and the hybrid baseline grid yield much higher drag for a given lift coefficient. One should further observe that, in Figs. 8 and 9, the authors have included two broken lines indicating variations of ± 150 drag counts with respect to the experimental value at the corresponding lift coefficient. It is clear in these figures that essentially all of the present calculations, with the clear exception of the SA results in the hybrid grid, fall within the

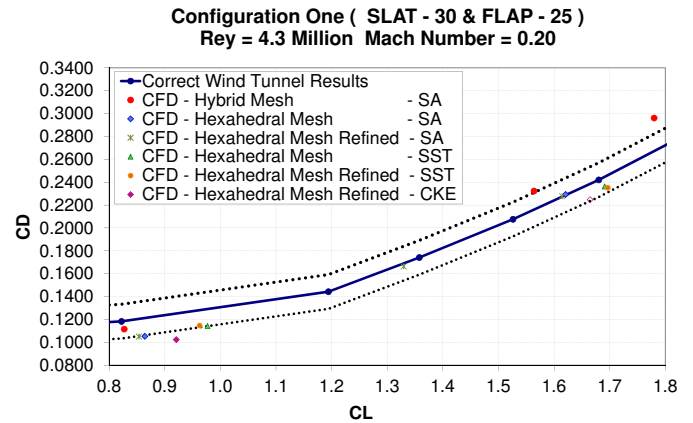


Fig. 8 Drag polars for configuration one without brackets (lower range of C_L).

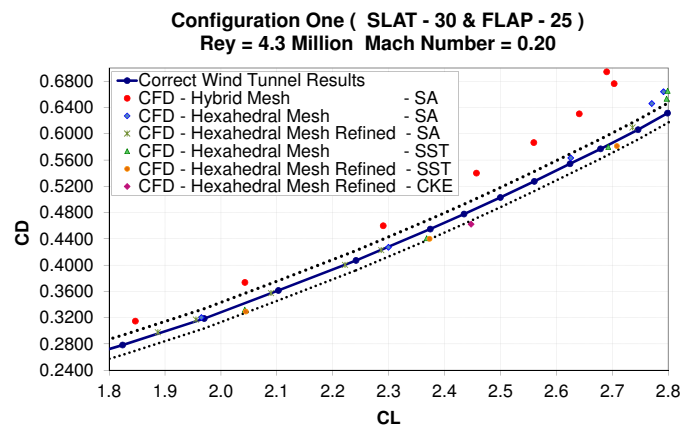


Fig. 9 Drag polars for configuration one without brackets (higher range of C_L).

150 drag count margins.

The flow pattern obtained for the simulations performed with the baseline hexahedral mesh and using the SST turbulence model are shown in Fig. 10. The vortex structure over the flap trailing edge and near the pod junction is considerably smaller than those obtained by the simulations performed with the SA turbulence model for the same grid. The increase in the angle of attack leads, for the SST solutions, to a decrease in the size of this vortex structure until it disappears. Thus, one can observe the topology of the flow solutions obtained is quite dependent on the adopted turbulence model.

ON THE EFFECTS OF TURBULENCE MODELING AND GRID REFINEMENT ON HIGH-LIFT CONFIGURATION AERODYNAMIC SIMULATIONS

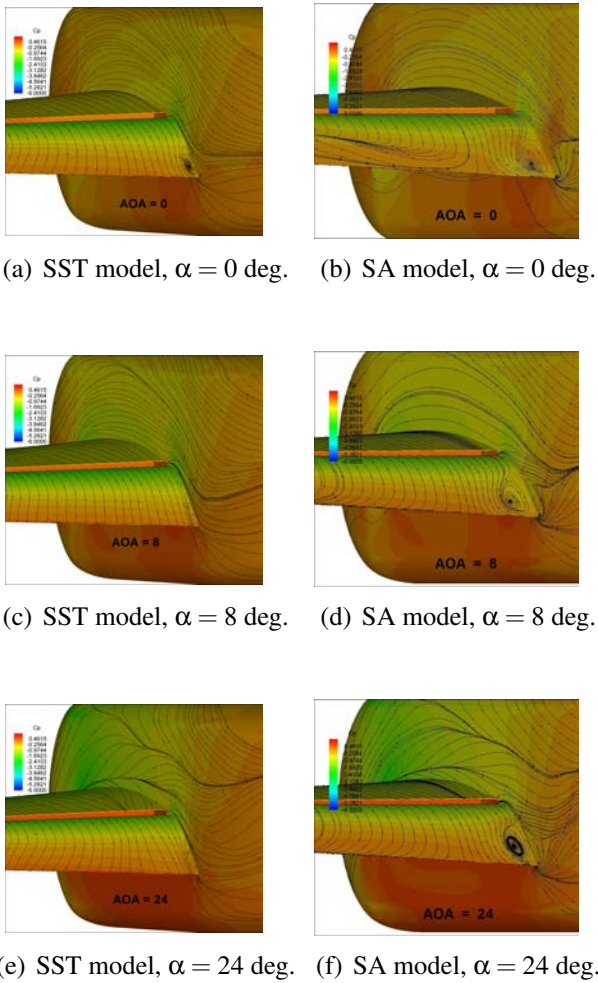


Fig. 10 Shear lines over configuration *one* for three angles of attack - Hexahedral Mesh - SST and SA Models.

5 Configuration With Supporting Brackets

The lift curves in Fig. 11 are a summary of all the lift coefficient results obtained for the configuration with brackets. One can see in this figure the C_L versus AoA curves for the calculations with the SA model in all three meshes, results for the SST model in the medium mesh, and, also, the effect of computing a new lift point restarting from a previous calculation at a smaller angle of attack. It should be pointed out that, for most of the calculations in the present work, for a given flight condition, the computations are started from freestream conditions. However, in

a few cases, the restart procedure was also considered in order to initialize the numerical simulation of the next higher angle of attack from a converged solution a smaller value of α .

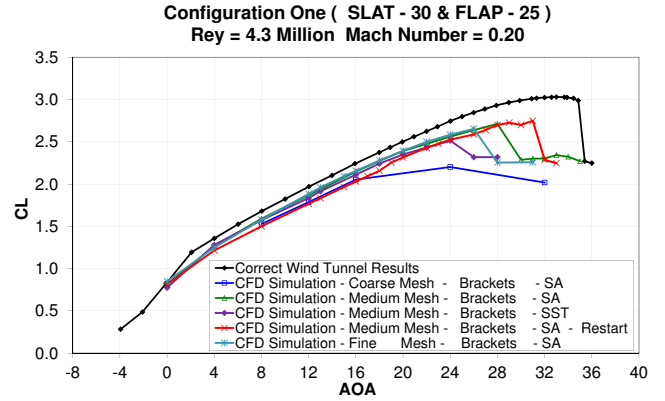


Fig. 11 Comparison of C_L versus AoA curves for the configurations with brackets.

In Fig. 11, one can observe that the computational results, for the all the performed simulations, are shifted with regard to the experimental data. In particular, the results obtained for the coarse mesh with the SA model present a very premature stall angle of attack and lower C_{Lmax} value than the other results. The simulations performed with the medium mesh, with the same SA model, provided an improvement in the capture of the lift coefficient, C_L , in relation to the results obtained with the coarse mesh. The stall is still premature, but it is now occurring at a higher angle of attack, more precisely at 28 deg. The increase in the stall angle of attack contributes to diminish the difference between the maximum experimental C_L and the one obtained by the numerical simulation. Moreover, the somewhat systematic shift observed between the experimental data and the simulation results is also decrease with the adoption of the medium mesh. Nevertheless, despite the improvements, the calculated $C_L \times \alpha$ curve and the value of C_{Lmax} obtained from the simulations are still not as close to the experimental data as one would like.

A comparison of the effects of the turbulence model used in the simulations is also performed for the calculations with the medium mesh. The results for the SA and SST models are very simi-

lar up to $AoA = 24$ deg., although the SST model computations yield slightly lower values of lift coefficient at each corresponding angle of attack than those obtained with the SA model. However, the calculations with the SST turbulence model indicate that the wing stalls at an angle of attack somewhere between 24 and 26 deg., whereas the results with the SA model only indicate stall above $AoA = 28$ deg. As it is clear from the figure, both calculations yield a premature stall when compared to the experimental data. Nevertheless, the results with the SA model are much closer to the experimental data in the high angle of attack range.

The results obtained with the same medium mesh, but now considering the simulation from a previously converged solution at a smaller angle of attack, yield smaller values of C_L , for the same angle of attack, than the results obtained starting the simulations from freestream conditions, which are referred to as solutions starting “from scratch”. On the other hand, the results obtained starting the computations from freestream conditions yield an earlier stall than when using the restart approach. In other words, the adoption of the restart approach led to a 3 deg. increase in the computed value of the stall angle of attack and, also, to a small increment in the computed value of $C_{L_{max}}$. Hence, this approach yields $C_{L_{max}}$ and angle of attack for maximum C_L which are closer to the experimental data.

The results with the SA model and the fine mesh were disappointing. As previously discussed, the fine grid was generated from a volumetric refinement of the medium grid and, hence, one would expect that this would improve the ability of capturing off-body flow structures. However, as one can see in Fig. 11, the calculations with the fine grid are indicating a more premature stall than that obtained with the medium mesh. For the lower values of angle of attack, the results in the fine mesh are identical to those obtained in the medium grid.

Figure 12 shows the C_D versus C_L curves, for the calculations with the brackets. It can be observed that the present calculations, with the coarse grid, yield results which are, somewhat,

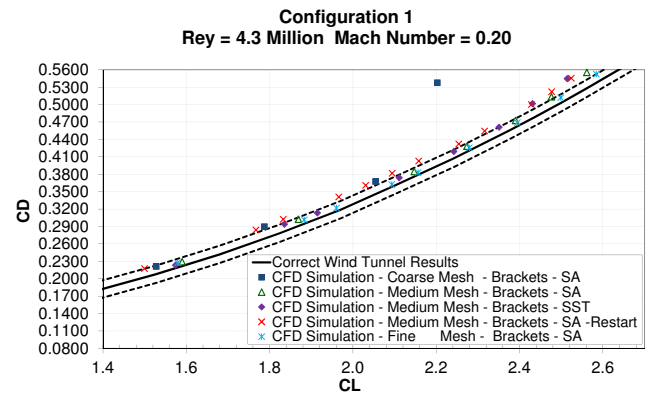


Fig. 12 Comparison of polar curves for the configurations with brackets.

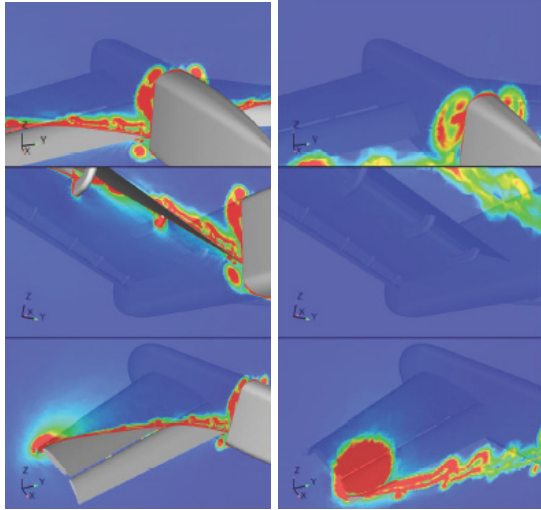
outside the ± 150 drag count range around the experimental values. In some sense, this is to be expected because the present calculations considered only two mesh elements to represent the trailing edge of the high-lift configuration. Previous calculations for the configuration without brackets [6] have demonstrated that mesh refinement at the trailing edge is a must in order to achieve a better comparison of drag results with the experimental data. The reason for not inserting more mesh elements at the trailing edge, in the present calculations, is that such approach would yield meshes which would be beyond what the resources available at the time for the authors could handle.

In Fig. 12, one can also see the results obtained for the configuration with both the medium and fine meshes. The drag results in the medium mesh, for both SA and SST turbulence models, are close to each other, and in better agreement with the experimental data than the results in the coarse mesh. However, computations in the medium mesh, and using the restart initialization option, led to drag results which are also outside the ± 150 drag count range around the experimental data. Finally, the calculations performed in the fine mesh have yielded drag values closer to the experimental data than all the other computations here performed for the configuration with the supporting brackets.

Figure 13 presents two planes perpendicular to the aircraft longitudinal axis, colored by vor-

ON THE EFFECTS OF TURBULENCE MODELING AND GRID REFINEMENT ON HIGH-LIFT CONFIGURATION AERODYNAMIC SIMULATIONS

ticity magnitude. These plots attempt to help visualize the growth of the boundary layer over the configuration and the formation of the free shear layers behind the wing. These results were com-



(a) Plane over the wing. (b) Plane downstream of the wing.

Fig. 13 Vorticity magnitude contours along two x -planes over and downstream of the wing.

puted for the medium mesh and using the SA turbulence model. Moreover, the vorticity magnitude planes shown are for the configuration with brackets at 24 deg. of angle of attack. The wing tip vortex is clearly visible in the plots, as well as the perturbation created by the supporting brackets in the flow downstream of the wing.

6 Concluding Remarks

The present paper was interested in performing simulations for the NASA Trapezoidal Wing including the effects of the high-lift device supporting brackets. The objective was to study effects of turbulence model, mesh refinement and mesh topology in the quality of the results obtained. Such study is a parallel to an investigation already performed for the configuration without the supporting brackets, but with a limited number of turbulence models.

For the calculations without the brackets, the simulations with both hexahedral meshes have

indicated that the SA and SST results are somewhat equivalent. This is true for lift coefficient calculations as well as for the drag polars. For these cases, the present calculations yielded a value of $C_{L_{max}}$ which is slightly smaller than indicated by the experimental data, but the angle of attack for $C_{L_{max}}$ is correct. Calculations with the SA model in a coarse hybrid mesh have yielded results which were quite poor. Finally, calculations on the refined hexahedral mesh, and using a cubic $k - \epsilon$ model, improved the value of $C_{L_{max}}$, but at the expense of increasing the stall angle of attack beyond the correct experimental value.

Calculations have been performed for the configuration with the supporting brackets using three different grids. Results on the coarse grid were calculated solely with the SA model. The lift coefficient results for the coarse grid predicted a quite premature stall when compared to the experimental data. Drag calculations on the coarse grid are outside a range of ± 150 drag counts about the experimental data. Lift coefficient results in the medium and fine meshes, for the SA calculations are identical up to 26 deg. in angle of attack. However, the fine grid calculations stall beyond this angle of attack, whereas the medium grid results show an increase in the lift coefficient up to $\alpha = 28$ deg. Calculations with the SST model in the medium grid also present a lift curve which is similar to the ones obtained with the SA model, except that the maximum lift condition is achieved at 24 deg. in angle of attack.

Acknowledgments

The authors acknowledge the partial support of Conselho Nacional de Desenvolvimento Científico e Tecnológico, CNPq, under the Research Project Grants No. 312064/2006-3 and No. 471592/2011-0. Fundação de Amparo à Pesquisa do Estado de São Paulo, FAPESP, has also provided partial support for the present work under FAPESP Grant No. 2011/12493-6, and such support is also greatly appreciated.

References

- [1] Johnson, T.F., and Tinoco, E.N., “Thirty Years Of Development and Application of CFD at Boeing Commercial Airplane Seattle,” *Computers & Fluids*, Vol. 34, No. 10, Dec. 2005, pp. 1115-1151.
- [2] Vos, J.B., Rizzi, A., Darraq, D., and Hirschel, E.H., “Navier-Stokes Solvers in European Aircraft Design,” *Progress in Aerospace Sciences*, Vol. 38, No. 8, Nov. 2002, pp. 601-697.
- [3] Chaffin, M., and Pirzadeh, S., “Unstructured Navier-Stokes High-Lift Computations on a Trapezoidal Wing,” AIAA Paper No. 2005-5084, *Proceedings of the 23rd AIAA Applied Aerodynamics Conference*, Toronto, Canada, Jun. 2005.
- [4] Johnson, P., Jones, K.M., and Madson, M., “Experimental Investigation of a Simplified 3D High-Lift Configuration in Support of CFD Validation,” AIAA Paper No. 2000-4217, *Proceedings of the 18th AIAA Applied Aerodynamics Conference and Exhibit*, Denver, CO, Aug. 2000.
- [5] Antunes, A.P., da Silva, R.G., and Azevedo, J.L.F., “A Study of Different Mesh Generation Approaches to Capture Aerodynamic Coefficients for High-Lift Configurations,” *Proceedings of the 27th International Congress of the Aeronautical Sciences – ICAS 2010*, Nice, France, Sept. 2010.
- [6] Antunes, A.P., Azevedo, J.L.F., and da Silva, R.G., “Numerical Simulations of Turbulent Flow over a High-Lift Configuration,” AIAA Paper No. 2011-3006, *Proceedings of the 29th AIAA Applied Aerodynamics Conference*, Honolulu, HI, June 2011.
- [7] van Dam, C.P., “The Aerodynamic Design of Multi-Element High-Lift Systems for Transport Airplanes,” *Progress in Aerospace Sciences*, Vol. 38, No. 2, Feb. 2002, pp. 101-114.
- [8] Payne, F.M., Wyatt, G.W., Bogue, D.R., and Stone, R.C., “High Reynolds Number Studies of a Boeing 777-200 High-Lift Configuration in the NASA ARC 12’ Pressure Tunnel and NASA LaRC National Transonic Facility,” AIAA Paper No. 2000-4220, Denver, CO, Aug. 2000.
- [9] Rogers, S.E., Roth, K., Nash, S.M., Baker, M.D., Slotnick, J.P., Whitlock, M., “Computational of Viscous Flow for a Boeing 777 Aircraft in Landing Configuration,” AIAA Paper No. 2000-4221, *Proceedings of the 18th AIAA Applied Aerodynamics Conference and Exhibit*, Denver, CO, Aug. 2000.
- [10] Eliasson, P., “CFD Improvements for High-Lift Flows in the European Project EUROLIFT,” AIAA Paper No. 2003-3795, *Proceedings of the 21st AIAA Applied Aerodynamics Conference*, Orlando, FL, Jun. 2003.
- [11] Rudnick, R., “CFD Assessment for High-Lift Flows in the European Project EUROLIFT,” AIAA Paper No. 2003-3794, *Proceedings of the 21st AIAA Applied Aerodynamics Conference*, Orlando, FL, Jun. 2003.
- [12] Metacomp Technologies Inc., CFD++, “<http://www.metacomp.tech.com/>”.
- [13] Spalart, P.R., and Allmaras, S.R., “A One-Equation Turbulence Model for Aerodynamic Flows,” AIAA Paper No. 92-0439, *30th AIAA Aerospace Sciences Meeting and Exhibit*, Reno, NV, Jan. 1992.
- [14] Menter, F.R., “Two-Equation Eddy-Viscosity Turbulence Models for Engineering Applications,” *AIAA Journal*, Vol. 32, No. 8, Aug. 1993, pp. 1598-1605.
- [15] Palaniswamy, S., Goldberg, U., Peroomian, O., and Chakravarthy, S., “Prediction of Axial and Transverse Injection into Supersonic Flow,” *Flow, Turbulence and Combustion*, Vol. 66, No. 1, Jan. 2001, pp. 37-55.
- [16] Ansys Inc., “<http://www.icemcfd.com/>”.
- [17] http://hiliftpw.larc.nasa.gov/98-99WebArchive-WithMods/links/fslf/config01_re03_avg_force.txt

Copyright Statement

The authors confirm that they, and/or their company or organization, hold copyright on all of the original material included in this paper. The authors also confirm that they have obtained permission, from the copyright holder of any third party material included in this paper, to publish it as part of their paper. The authors confirm that they give permission, or have obtained permission from the copyright holder of this paper, for the publication and distribution of this paper as part of the ICAS2012 proceedings or as individual off-prints from the proceedings.